



Contents lists available at ScienceDirect

Chemical Engineering Journal

journal homepage: www.elsevier.com/locate/cej

Self-powered broadband photodetection with mixed-phase black TiO₂-assisted output boosting of a biobased triboelectric nanogenerator

Ishita Chakraborty^{a,1}, Ming-Chung Wu^{b,c,d,1}, Sz-Nian Lai^e, Chao-Sung Lai^{a,f,g,h,*}

^a Department of Electronic Engineering, Chang Gung University, Guishan District, Taoyuan City 33302, Taiwan

^b Department of Chemical and Materials Engineering, Chang Gung University, Guishan District, Taoyuan City 33302, Taiwan

^c Green Technology Research Center, Chang Gung University, Guishan District, Taoyuan City 33302, Taiwan

^d Division of Neonatology, Department of Pediatrics, Chang Gung Memorial Hospital at Linkou, Guishan District, Taoyuan City 33305, Taiwan

^e Department of Materials Science and Engineering, National Tsing Hua University, Hsinchu 30010, Taiwan

^f Department of Nephrology, Chang Gung Memorial Hospital at Linkou, Guishan District, Taoyuan City 33305, Taiwan

^g Department of Materials Engineering, Ming Chi University of Technology, Taishan District, New Taipei City 24301, Taiwan

^h Artificial Intelligent Innovation Research Center, Chang Gung University, Guishan District, Taoyuan City 33302, Taiwan

ARTICLE INFO

Keywords:

Triboelectric nanogenerator
Dielectric polymer
Photoelectrons
Self-powered
Photodetection
Circular bioeconomy

ABSTRACT

Simultaneously harvesting vibrating energy and solar energy from the ambient environment through triboelectric nanogenerators (TENGs) to construct a self-powered system is fascinating and exacting work. In this study, photoinduced biobased triboelectric generation during friction between a PDMS@black TiO₂ nanocomposite film and a chemically treated human hair film was demonstrated. The triboelectric output voltage and current signals were intensified by approximately 1.2–2.2 times, with output maxima of 85 V and 3.5 μA after illumination under full-spectrum conditions. Upon illumination, the output signals of the TENGs were appreciably altered depending on the intensity and wavelength of the light, delivering superior photoresponse characteristics, which included an outstanding responsivity of 606.8 V W⁻¹ and an ultrabroad detection range that extended over the ultraviolet (UV), visible and near-infrared (IR) regions, thereby providing a novel route for energy harvesting devices. These devices, along with self-powered photodetectors, ameliorate other environmental issues by eliminating human hair waste and developing a closed-loop system that promotes the responsible use of resources.

1. Introduction

Triboelectric nanogenerators (TENGs), developed based on the integration of triboelectrification and electrostatic induction, have been demonstrated to be cost-effective, simple, and efficient devices capable of operating as self-powered smart devices and harvesting energy in different working modes for use in a wide range of application frameworks, such as natural mechanical vibration, regular human motion, water waves, wind and light [1–3]. They are attracting worldwide attention owing to the rapid advancement of self-powered system applications, small portable electronics, and wireless sensing networks. For fruitful commercialization of these prospective applications, TENGs with superior conversion efficiency are needed. Various approaches to upgrade the conversion efficiency of TENGs have been reported, such as selection of appropriate triboelectric materials [4], control of the surface

morphology [5], charge injection [6], and postprocessing [7]. Among all the aforementioned strategies, selection of materials is the most efficacious technique to fundamentally enhance the performance of TENGs via improvement of the surface charge density. In general, any material with recognizable charge affinity might be utilized to fabricate a TENG, which results in a wide range of materials at opposite ends of the triboelectric series that can exhibit outstanding performance. In particular, polytetrafluoroethylene (PTFE) [8] and polydimethylsiloxane (PDMS) [9] are widely accepted tribomaterials for achieving net negative triboelectric charges, while nylon [10] and metal [11] are widely used tribomaterials for acquiring net positive charges. Additionally, some nanostructured materials are utilized in semiconductor/polymer-based TENGs to improve the effective contact area as well as the dielectric properties, such as CaCu₃Ti₄O₁₂ nanoparticles [12] and barium titanate nanoparticles [13]. Remarkably,

* Corresponding author.

E-mail address: cslai@mail.cgu.edu.tw (C.-S. Lai).

¹ These authors contributed equally to this work.

<https://doi.org/10.1016/j.cej.2022.139138>

Received 3 June 2022; Received in revised form 6 September 2022; Accepted 7 September 2022

Available online 11 September 2022

1385-8947/© 2022 Elsevier B.V. All rights reserved.

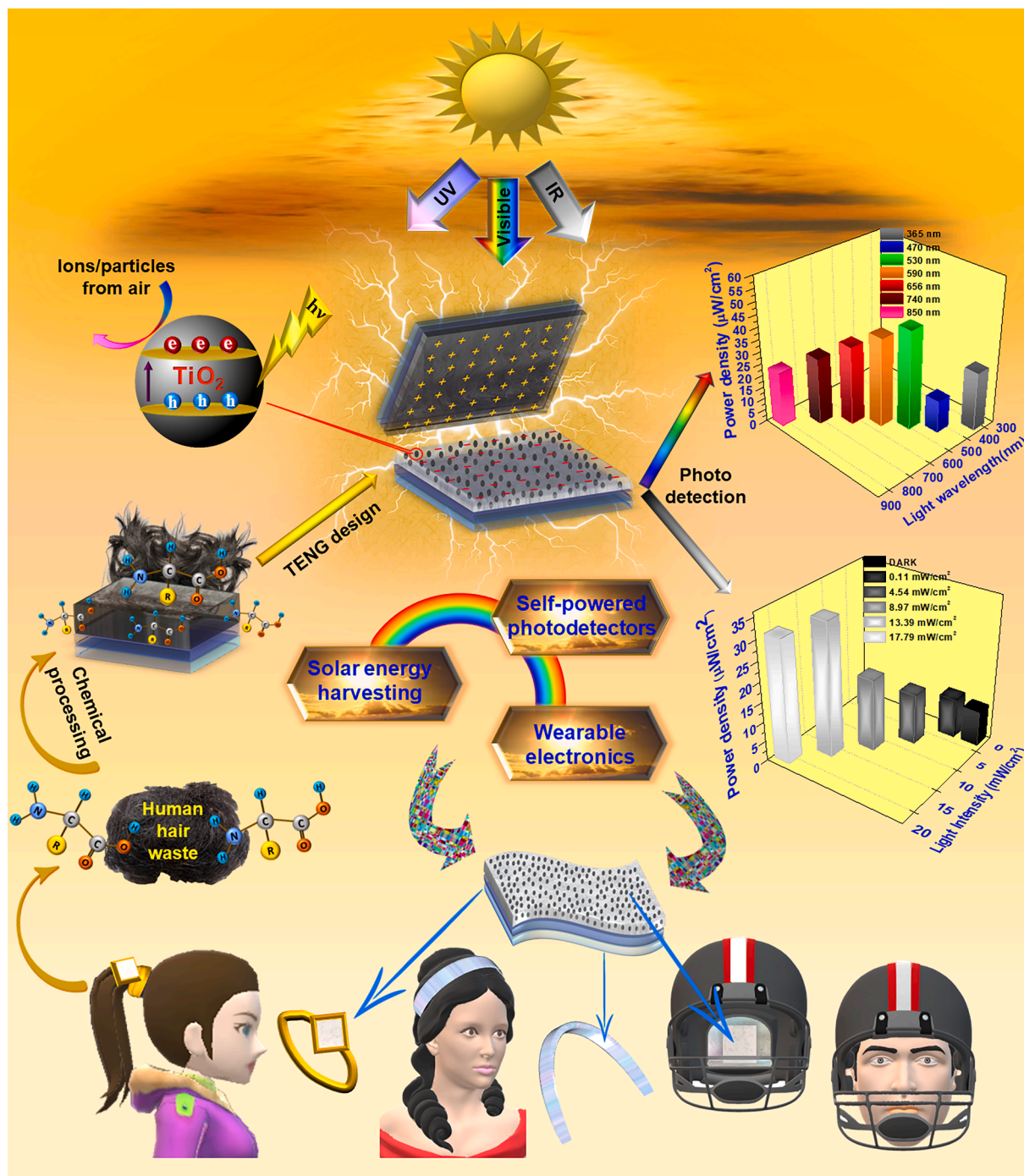


Fig. 1. Schematic illustration of the TENG based on the PDMS@BTN nanocomposite film and human hair as a circular material, adding desirability to the circular bioeconomy with human hair waste.

studies have also illustrated that the output signals of TENGs can be varied due to the superlative photoelectric properties of semiconductor materials induced by solar radiation absorption [14–18]. In 2015, Su et al., reported a perovskite-based self-powered photodetector by employing the mutual properties of the triboelectric effect and photoelectric effect, which was ascribed to alteration of the photoconductivity and the surface charge density of the MAPbI₃-based composite thin film under of solar light illumination [15]. In 2019, Han et al., demonstrated photoinduced signal intensification and polarity reversal controlled by surface trapped charges in a TENG comprising an ultrathin Au film and a TiO₂ layer as friction materials [16]. In 2021, Yu et al., reported another approach for photoenhanced TENGs owing to the wide absorption

characteristics of bismuth oxyiodide, which utilized the existence of deep surface states attributable to the dangling bonds and traps within bismuth oxyiodide [17].

The discovery of the novel nanomaterial black TiO₂ nanoparticles (BTNs) has garnered substantial interest because of its appreciable optical absorption in the ultraviolet (UV)- visible spectrum, endowing it with good prospects in solar-driven applications [19]. Previous research demonstrated a simple method to synthesize BTNs by inducing oxygen vacancies at the surface of titanium, and the material showed outstanding photocatalytic activity under visible light illumination without introducing lattice doping or surface decoration [20]. However, considering that energy consumption is a very important characteristic

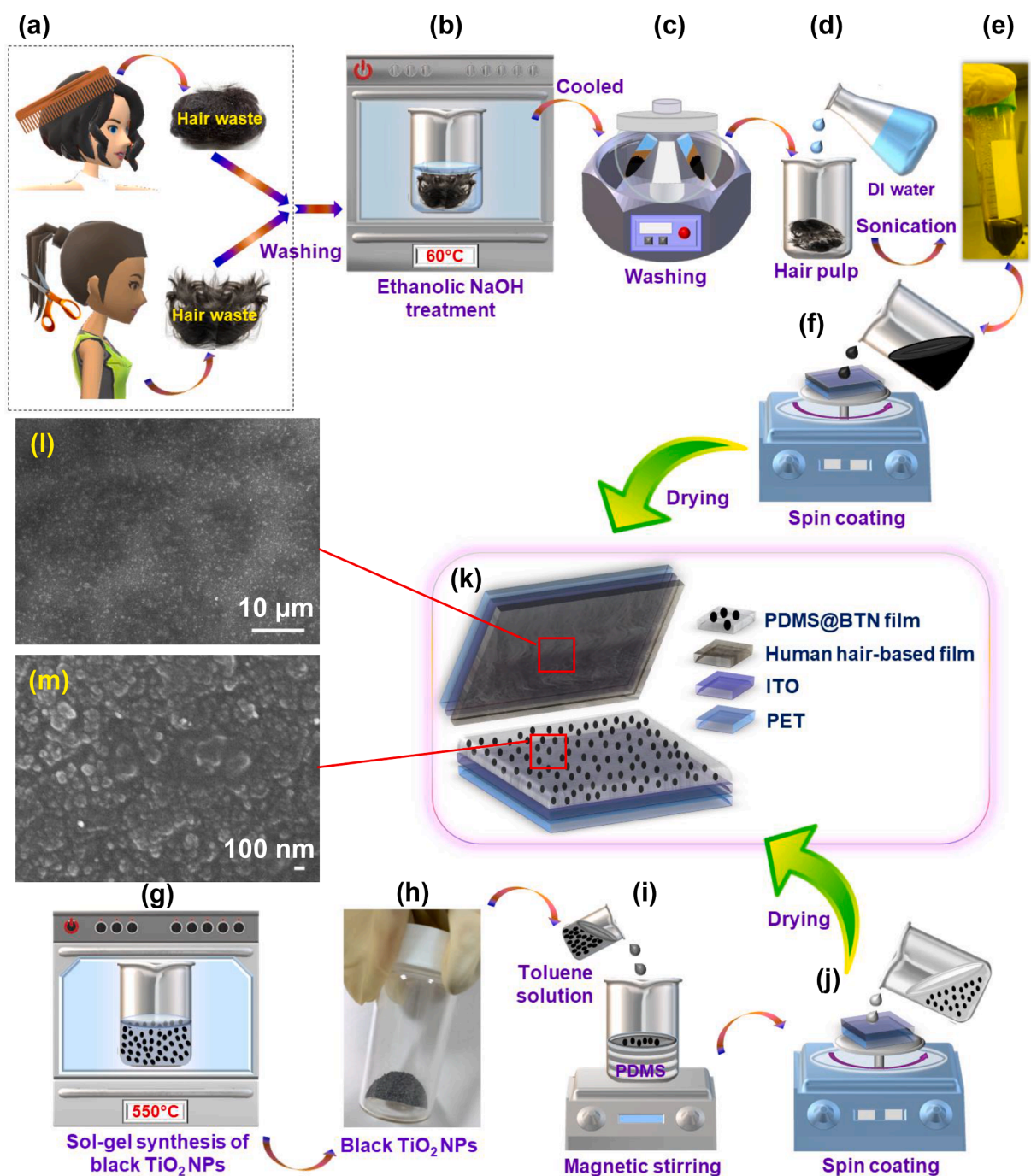


Fig. 2. Schematic illustration of the fabrication process for the TENG comprising a chemically treated human hair film (positive tribolayer) (a-f) and a PDMS@BTN film (negative tribolayer) (g-j). (k) Structural diagram of the TENG. FE-SEM images of the (l) chemically treated human hair film and (m) PDMS@BTN-2 film.

of any electronic device, this process requires further upgrades to attain sustainability. Thus, the latest research has concentrated on the global power consumption, which is the most important but seldom examined key requirement for photodetectors. Recently, self-powered photo-detection from the UV to visible regions has attracted immense attention because of its major importance in safeguarding human health and the environment and in related scenarios. Some of the existing strategies to effectively improve the photoresponse performance include triboelectric voltage-induced polarization and driving oxygen vacancies to accumulate at the contact interface, hence reducing the Schottky barrier height (SBH) [21] and the light-induced surface charge density variation [15,22]. Thus, the surface states play a crucial role in the photodetection mechanism. Human hair exhibits intense positive triboelectricity, but

fabricating natural hair-based practical TENG devices capable of exhibiting stable output signals by processing hair into a uniformly stacked friction layer is a great challenge. Consequently, there are very limited studies presenting human hair as an active material to fabricate stable and high-performance TENGs [23,24].

Herein, we report photostimulated triboelectric generation by introducing BTNs with trivalent titanium ions, structural defects, and oxygen vacancies, showing extraordinarily high absorbance in the UV-visible light spectrum [19], to design a photoinduced TENG based on a PDMS@black TiO₂ nanocomposite film and a chemically treated human hair film as friction materials to concurrently harvest vibrating mechanical energy and solar energy. Electron excitation by photon absorption alters the probability of effective electron transfer in the

contact; thus, compared with dark conditions, a considerable increase in the output signal of the TENG is observed under light illumination. By using Kelvin probe force microscopy (KPFM) measurements, we present an innovative mixed-phase BTN-assisted double sensing module in which both the photoconductivity and the surface charge density of the PDMS@black TiO₂ nanocomposite film are remarkably changed upon light irradiation. The utilization of human hair allows the fabrication of cost-efficient biobased TENGs with a tribomaterial that is abundant but considered a slowly degrading waste material without a proper circular recycling system for elimination, recovery and regeneration, thus alleviating the issue in waste management systems [23]. Therefore, emphasis should be placed on developing systematic utilization of human hair-based waste, which is noticed in municipal waste streams almost everywhere in the world, to ensure social and environmental well-being. This work contributes to an innovative approach for fabricating cost-effective and high-efficiency energy harvesting devices constructed as an auspicious green energy source for the circular bioeconomy (Fig. 1) as well as a new way to fabricate high-performance self-powered and ultrabroadband photodetectors. This integral approach of developing a self-powered broadband photodetection system while utilizing waste material shows great potential in harvesting energy, photodetection, easing the challenges in waste management regarding problematic waste and mitigating environmental pollution. Therefore, it is expected to be considered a novel initiative toward environmental, economic and social sustainability.

2. Experimental section

2.1. Chemical treatment of human hair waste and human hair-based film fabrication

Initially, 1.50 g of hair waste (scalp hair waste samples of 20–30-year-old Asian women) was rigorously washed with ethanol (Honeywell, ≥99.8 %) and DI water to remove all the dirt and impurities, followed by drying at 60 °C for approximately 30 min. This clean hair sample was immersed in 1.50 M ethanolic NaOH (SHIMAKYU'S PURE CHEMICALS) solution (40 mL) and heated at 60 °C for 12 h, keeping it sealed. Then, it was allowed to achieve room temperature naturally, followed by washing the processed hair mush with ethanol through centrifugation, and it was dissolved in DI water (in an equal amount) to prepare a homogeneous solution. As depicted in Fig. 2a-f, a uniform film of 12.5 μm thickness was developed by depositing (spinning at 1500 rpm for 40 s) the as-produced homogeneous solution onto an ITO-coated polyethylene terephthalate (PET) substrate using the spin coating technique to develop the positive side of the TENGs. Before spin coating, the surface of the ITO-coated PET substrate was cleaned by a nitrogen spray gun, and the as-fabricated film was dried at 60 °C for 5.0 h after spin coating. The detailed fabrication procedure of the human hair-based film is precisely explained in our previous study, Reference [14].

This experiment was performed in accordance with The Code of Ethics of the World Medical Association (Declaration of Helsinki) for experiments involving human subjects and approved by the Human Test Ethics Committee of Chang Gung Medical Foundation (Application No.-2109220003, Date- 24 September 2021). Informed consent was obtained from all the donors for inclusion of the waste hair samples that they donated before they participated in the study.

2.2. Preparation of black and white TiO₂ nanoparticles

The sol-gel method was used for the synthesis of BTNs and white TiO₂ nanoparticles. Initially, 7.20 mL of titanium isopropoxide (Ti(OCH(CH₃)₂)₄, ACROS, 98+%) was mixed with 21.60 mL of *n*-propanol (C₃H₇OH, Fisher, reagent grade) at ambient temperature, followed by the addition of 1.00 mL of hydrochloric acid (HCl, ACROS, 37 %) and 1.00 mL of deionized water to begin the gelation process. Then, the Ti-O precursor gel was calcined at 550 °C under argon flow (99.995 %) or air

flow (21 % O₂ in N₂) for 2.0 h to acquire BTNs and white TiO₂ nanoparticles (WTNs). The synthesis procedure of the TiO₂ nanoparticle series is explained in detail in one of our previous studies, Reference [19].

2.3. Fabrication of the unmodified PDMS film and PDMS@TiO₂ nanocomposite films

To prepare the PDMS source solution, the Sylgard 184 elastomer (DOW CORNING, USA) was mixed with the curing agent (10:1 proportion) through magnetic stirring. Then, this solution was deposited (at 2500 rpm for 60 s) onto ITO-coated PET using a spin coater, and the as-prepared film was cured at 80 °C for 2.0 h. As shown in Fig. 2h-j, to fabricate the PDMS@BTN nanocomposite film on a PET substrate with ITO working as the electrode material, the as-synthesized BTNs dispersed in toluene were mixed into the same PDMS source solution by magnetic stirring for approximately 3.0–4.0 h until the solution became free from bubbles. For comparative analysis, PDMS@BTN nanocomposite films were fabricated with three different weight percentages of BTNs; these samples are henceforth denoted PDMS@BTN-1 (0.060 wt % BTNs), PDMS@BTN-2 (0.077 wt% BTNs) and PDMS@BTN-3 (0.090 wt% BTNs). To construct the negative triboelectric layers, the above prepared homogeneous solutions were spin-coated (at 1200–2100 rpm for 60 s) onto the clean (cleaned by a N₂ gun) surface of a 3.0 × 3.0 cm² ITO-coated PET substrate and subsequently cured at 80 °C for 2.0 h. Further curing at 115 °C for 2.0–3.5 h was essential for the PDMS@BTN nanocomposite film (with 38.6 μm thickness) to remove toluene. Following similar fabrication steps, a PDMS@white TiO₂ nanocomposite film (0.077 wt% WTNs) was also prepared over the same substrate and electrode for the sake of comparative study and is referred to as PDMS@WTN.

2.4. Fabrication of the TENG-based photodetector device

The TENG-based self-powered photodetector device was constructed by assembling the as-fabricated PDMS@BTN nanocomposite-based negative friction layer and the chemically treated waste hair film-based positive friction layer, both developed on transparent ITO-coated PET substrates. In the final step, Cu wires were attached to the electrodes to measure the performance of the as-fabricated TENGs. These TENGs (Fig. 2k) with a total contact area of 3.0 × 3.0 cm² were operated in vertical contact-separation mode under both dark and illumination (with different wavelengths and intensities) conditions.

2.5. Characterization and measurement

The crystal structure was studied using X-ray diffraction (XRD, Rigaku_TTRAX III diffractometer equipped with a Cu Kα source). The surface morphologies and elemental composition of the as-prepared samples were investigated using field emission scanning electron microscopy (FE-SEM) integrated with energy-dispersive spectroscopy (EDS) (FE-SEM, JEOL JSM-7500F) and atomic force microscopy (AFM, Innova B067, Bruker Corp. USA). Field-emission transmission electron microscopy (FE-TEM, JEM-ARM200FTH, Japan) was employed to detect the microstructures of BTNs and WTNs. A Fourier-transform infrared spectrometer with an attenuated total reflection (ATR) microscopy accessory (Germany Bruker, Vertex 80v) was used to investigate the chemical bonding of the PDMS@BTN nanocomposite films and chemically treated human hair film. The UV-vis spectra of BTNs and WTNs were studied using a UV/Vis spectrophotometer (Jasco, V-650, Japan), measured from 300 to 900 nm. An alpha stepper (DektakXT, Bruker) was used to acquire the thickness of the PDMS@BTN nanocomposite films and the chemically treated human hair film. Surface charge potential measurements were performed using KPFM (Dimension-3100 Multimode, Digital Instruments). The electrical output voltage and current signals of the as-fabricated TENGs were measured by using a Keithley 6514 programmable electrometer and a low-noise

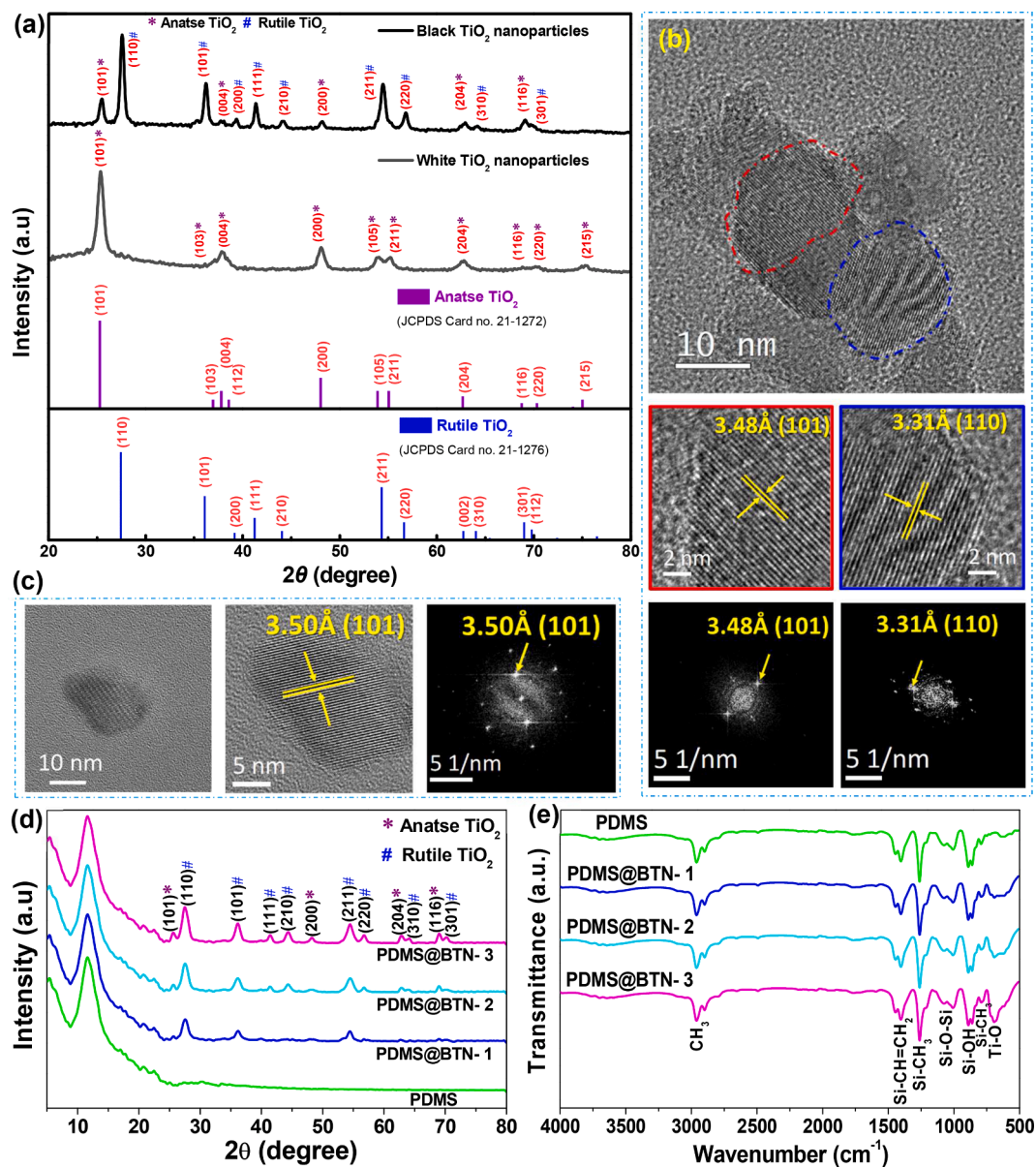


Fig. 3. (a) XRD patterns of WTNs and BTNs. TEM images with magnified high-resolution TEM (HRTEM) images of TiO₂ nanocrystals and corresponding fast Fourier transformed patterns for (b) BTNs and (c) WTNs. (d) XRD patterns of PDMS and PDMS@BTN nanocomposites. (e) FTIR spectra of PDMS and PDMS@BTN nanocomposites.

current preamplifier (Stanford Research System Model SR570). The TENGs were illuminated by a tunable LED light source (MIGHTEX, Uninanotech UNI-EGF-LED). The dielectric properties of the pure PDMS and PDMS@BTN nanocomposite films were studied using an Agilent B1500A semiconductor device parameter analyzer.

3. Results and discussion

As shown in Fig. 2k, the as-fabricated TENGs consist of two separate parts: The lower part is a PDMS film with BTNs embedded in it that functions as an efficacious light absorber and is developed on a transparent ITO-coated PET substrate. The upper part is assembled with a chemically treated human hair film regarded as a highly triboelectric material coated on the same substrate, characterizing the proposed TENG device as a biobased TENG. ITO layers act as both the lower and upper electrodes and are connected to the negative and positive terminals of the measurement system for data collection. FE-SEM and AFM were employed to identify the morphology and surface roughness of the

electrification layers. A top-view FE-SEM image giving the typical morphology profile of the PDMS@BTN-2 film is shown in Fig. 2m, validating that BTNs can be homogeneously dispersed in the PDMS matrix, while PDMS@BTN-1 exhibits enclosed structures of BTN clusters inside the PDMS matrix (Fig. S1b). With a further increase in the BTN amount in the PDMS@BTN nanocomposite to over 0.077 wt%, nanoparticles start agglomerating, as exhibited by Fig. S1c, presenting a top-view FE-SEM image of the PDMS@BTN-3 film. Fig. S1a demonstrates the surface morphology of the unmodified PDMS film, indicating that the flat film is free from any cracks or imperfections. The EDS spectra (Fig. S2 and Table S1) indicate the successful incorporation of BTNs into the pure PDMS film. The surface roughness of the PDMS@BTN nanocomposite films was found to improve with increasing nanoparticle content due to complete remodeling of the surface morphology (Fig. S3). The FE-SEM image in Fig. 2l shows that the film prepared by chemical treatment of the waste hair sample was quite uniform with complete coverage of the ITO electrode featuring a nanoisland structure morphology, thus elevating the surface roughness even without any

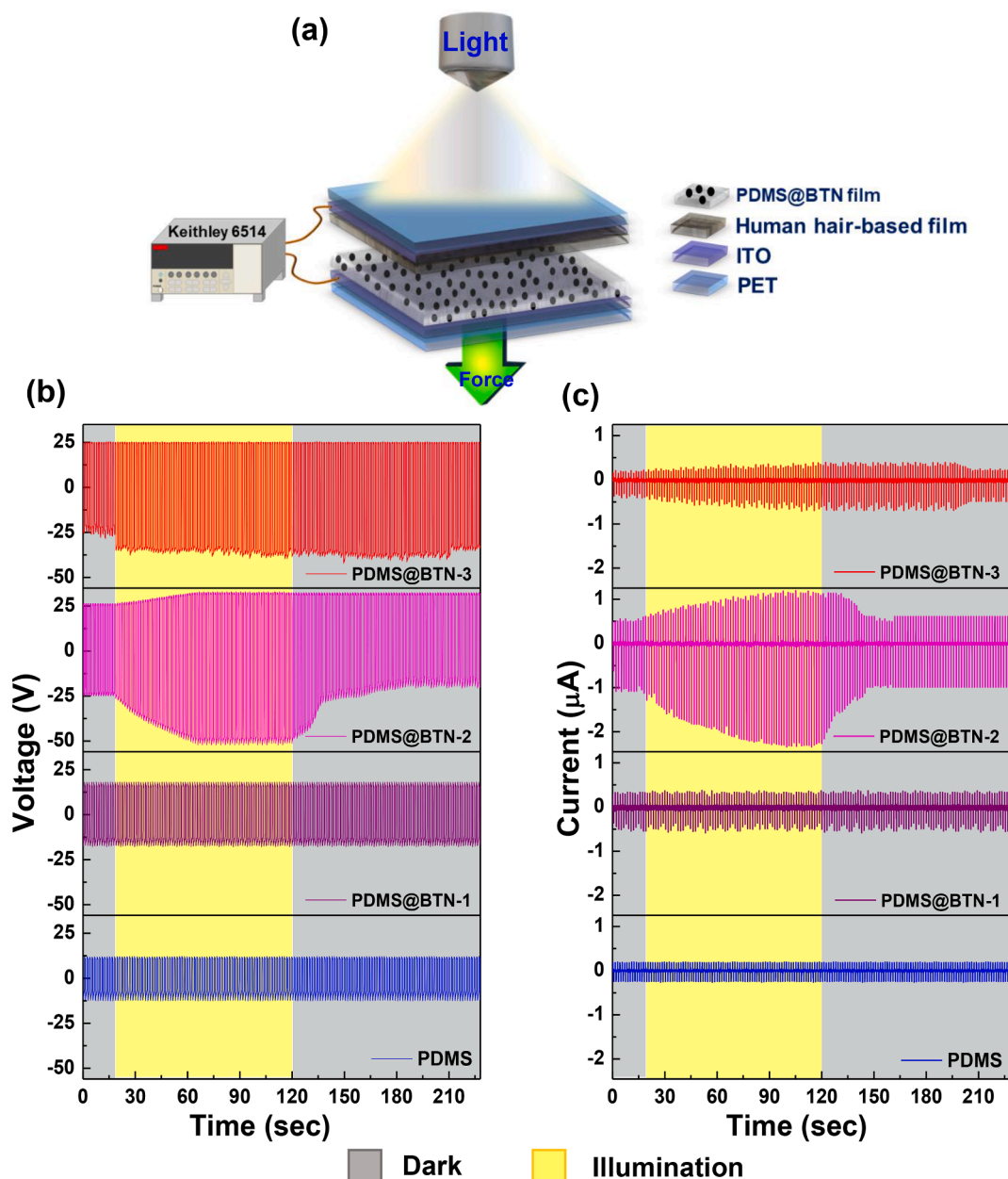


Fig. 4. (a) Schematic diagram of the measurement arrangement of the TENG upon illumination. (b) Voltage and (c) current outputs of PDMS and PDMS@BTN-based TENGs in the dark and under illumination.

cracks or evidence of undissolved hair fibers, as revealed by the AFM analysis result (Fig. S4a), which also well matches the FE-SEM image. The EDS analysis results (Table S2), comprising the weight and atomic percentage of each element present in the chemically treated human hair film, are consistent with previous results [25]. These results were also confirmed by Fourier-transform infrared (FTIR) spectroscopy analysis. The phase structures of the as-synthesized BTNs and PDMS@BTN nanocomposite films were investigated by XRD analysis (Fig. 3a,d). The XRD pattern of the BTNs presents a mixed phase, including anatase TiO_2 and rutile TiO_2 , while the WTNs only exhibit the anatase TiO_2 phase, as the disparate atmospheric heat treatments contribute to the origination of different TiO_2 crystal structures [19]. The diffraction peaks for BTNs gradually became more intense as the BTN content in the PDMS@BTN nanocomposite increased, maintaining the crystallinity of the composite films and the diffraction halo at approximately $2\theta = 12^\circ$, which indicates the amorphous microstructure of the PDMS [26]. The XRD pattern of the PDMS@WTN composite film

indicates successful incorporation of the WTNs into the PDMS matrix without the introduction of any deformation into the standard diffraction pattern of PDMS (Fig. S5). Fig. 3b shows a TEM image of the as-synthesized black TiO_2 nanocrystals, with an average particle size of 11.3 nm, while the size distribution histogram of the TiO_2 nanocrystals is demonstrated in Fig. S6. The lattice spacings of 3.31 and 3.48 Å for the as-synthesized black TiO_2 nanocrystals, shown in Fig. 3b, correspond to the (110) plane of rutile and the (101) plane of anatase, respectively. The coexistent phases of the BTNs are again confirmed in the fast Fourier transformed pattern (Fig. 3b), while the WTNs exhibit only the (101) plane of anatase, as presented in Fig. 3c.

As depicted in the FTIR spectra (Fig. 3e), the characteristic peak at approximately 689 cm^{-1} corresponds to bond formation in BTNs [27], which is not evident in the spectrum for the unmodified PDMS film but becomes more intense with the introduction of an increasing amount of BTNs into the pure PDMS to form PDMS@BTN nanocomposites. The absence of any new band in the FTIR spectra identifies the occurrence of

Table 1

Improvements in the output performance of the as-fabricated TENGs under illumination (white light) conditions.

| Sample | Improvement in output voltage | Response time | Recovery time |
|------------|-------------------------------|--|-------------------------|
| PDMS@BTN-1 | No | No | No |
| PDMS@BTN-2 | 68 % | 540–600 ms (1st response) 32 s (by definition) | 18 s (by definition) |
| PDMS@BTN-3 | 20 % | 810–1000 ms (1st response) (abrupt intensification) | 91 s (abrupt reduction) |

no chemical interactions between PDMS and BTNs.

Fig. S4b shows the FTIR spectrum for the chemically treated human hair film. A wide peak appears in the 3080–3557 cm^{-1} range, corresponding to the amide B band, amide A band (N–H stretch in resonance with the amide II overtone), and symmetric and asymmetric H–O–H stretching [28]. The characteristic peak of asymmetric CH_3 stretching is displayed at approximately 2965 cm^{-1} [28,24]. The appearance of bands between 1600 and 1700 cm^{-1} illustrates the amide I band, mostly the band components of the β region pleated structures confirming proteins, C=C stretching mode [29] and specifically H–O–H bending identified by the peak at 1645 cm^{-1} [28]; thus, the chemically treated human hair film presents the characteristic peak formed by the overlap of the N–H bending and C=C stretching vibration modes as a result of the formation of carboxylic acid by hydrolysis of amides after heating with ethanolic NaOH at 1637 cm^{-1} . The characteristic peaks of the symmetric and antisymmetric stretching modes of $-\text{COO}-$ are exhibited at 1573 cm^{-1} and 1396 cm^{-1} , respectively, which are due to the ionization of carboxylic acid groups in ethanolic NaOH medium [24]. The small peak appearing at approximately 1433 cm^{-1} arises from the CH_2 group scissoring mode vibration [24]. The sharp peak displayed at 1331 cm^{-1} represents S=O group formation, possibly because of the oxidation of cysteine disulfide cross-links existing in natural hair [24]. The processed hair film presents the characteristic peaks of the in-plane N–H bending mode of amide II at 1269 cm^{-1} and ester C–O asymmetric stretching at 1166 cm^{-1} [28]. The intense peak at 1047 cm^{-1} represents carbohydrate bonds [29]. The peak at 877 cm^{-1} exhibits the deformation of hydrocarbons in keratin proteins, and another strong peak at 670 cm^{-1} displays the C–OH out-of-plane bending vibration [24]. Thus, the FTIR spectrum shows a small distortion in the chemical structure of natural untreated hair, which was introduced by the strong base treatment at a certain temperature.

The charge generation performance of the TENGs was characterized by measuring their output voltage and current signals in the dark and under illumination conditions, as demonstrated in Fig. 4 and Table 1. The output performance of the as-fabricated transparent TENG devices comprising the tribopair of PDMS@BTN and human hair films was measured when operated in vertical contact-separation mode under white light on and off conditions. The dimensions of the device were $3 \times 3 \text{ cm}^2$, and the optimized effective area of the device that was illuminated during the data acquisition was approximately 4.45 cm^2 . A maximum separation distance of 30 mm between the upper and lower parts of the TENG device and an operation frequency of 0.7 Hz were maintained throughout the measurement. The whole measurement was performed under a repeated external force, which was applied through the movement of a linear stepper motor. An obvious improvement in the average peak-to-peak values of the output voltage and current even in the dark state can be detected after the introduction of BTNs (up to 0.077 wt%) into the PDMS matrix, and this is ascribed to the combined effect of the successfully developed special film morphology with elevated surface roughness [30] (Fig. 2m, Fig. S1 and Fig. S3),

improvement in the dielectric properties of the tribomaterial (Fig. 6c) [23,31] and significant reduction in the surface potential (Fig. 5a2-c2) with the incorporation of a small amount of highly dielectric BTNs. With a further increase in the BTN content in the composite film, a drop in the output signal was noted owing to the increase in the surface potential (Fig. 5a2-c2). Under dark conditions, the TENG output signal is entirely from the mechanical energy supplied by the periodic motion of the linear stepper motor, and the average peak-to-peak output voltage and current are only 36.3 V and 0.9 μA for PDMS@BTN-1, 52 V and 1.6 μA for PDMS@BTN-2, and 51 V and 0.6 μA for PDMS@BTN-3, respectively. When the white light is turned on, the PDMS@BTN-2-based TENG exhibits 1.7 times and 2.2 times improvements in the average peak-to-peak output voltage and current, respectively. The average peak-to-peak output voltage and current from the PDMS@BTN-3-based TENG represent enhancements of up to approximately 1.2 times and 1.9 times, respectively, whereas the PDMS@BTN-1-based TENG does not manifest any considerable change in the output signals (Fig. 4b,c). To elucidate the stability of the as-developed photodetector, we measured the photoresponse switching behavior under illumination conditions. We can observe that the PDMS@BTN-2-based TENG presents a first response time of 540–600 ms, and in the first response, it exhibits a 10.5 % increment in the output voltage. As presented in Fig. S8, this device shows a gradual increase in the output, which saturates at a value with a 68 % increment from the output voltage in the dark state. The time required to reach 90 % of the voltage deviation ($\Delta V = V_{\text{Light}} - V_{\text{Dark}}$) from 10 % of the voltage deviation was calculated to be 32 s. Therefore, following the convention for the response time estimation [32,33], the response time is determined to be 32 s. The PDMS@BTN-3-based TENG exhibits a slightly longer first response time (810–1000 ms), but it shows an abrupt increment in the output, and the increment in the output voltage is approximately 15.2 %. This increment is considerably lower than that of the PDMS@BTN-2-based TENG.

After the light is turned off, the time required for the output signal from the PDMS@BTN-2-based TENG to gradually decrease and recover to the original dark state signal is called the recovery time. Precisely, the recovery time is defined as the time required to reach 10 % of the output signal increment from 90 % of the output signal increment [32,33], and this value is 18 s for the PDMS@BTN-2-based TENG (Fig. S8), which is considered the recovery time. The peak-to-peak output voltage for the PDMS@BTN-3-based TENG shows an abrupt decrease approximately 91 s after turning off the light, nearly reverting to the original dark state voltage. Therefore, the recovery time for the PDMS@BTN-3-based TENG is approximately 91 s, which is much longer than that for the PDMS@BTN-2-based TENG.

This slow and higher response of the PDMS@BTN-2-based TENG is ascribed to the combined effect of the uniform distribution of nanoparticles in PDMS@BTN-2 (Fig. 2m) and the large surface-to-volume ratio of the BTNs (Fig. 3b and Fig. S6) along with the availability of more defects and trap states. This phenomenon results in a gradual but intense light interaction of the nanoparticles under irradiation [34,35].

Without illumination, the as-fabricated TENGs can transform vibrating energy into electricity during continual cycling [36], as shown in Fig. S9a-e. In the initial state, no charge transfer occurs between the PDMS@BTN nanocomposite film and chemically treated human hair film. After the human hair film comes into contact with the PDMS@BTN nanocomposite film, tribonegative charges accumulate on the PDMS@BTN nanocomposite film surface, while equal tribopositive charges accumulate on the human hair film surface. This phenomenon occurs due to electron transfer from the positive friction layer to the negative friction layer owing to the large differences in their electron affinities. Later, as the layers separate due to periodic cycling, the triboelectric charges generate a time-varying electric field in space and induce negative and positive charges on the upper and lower electrodes, respectively.

During this procedure, the inductive electrons flow from the lower to the upper ITO electrode through the external circuit to stabilize the

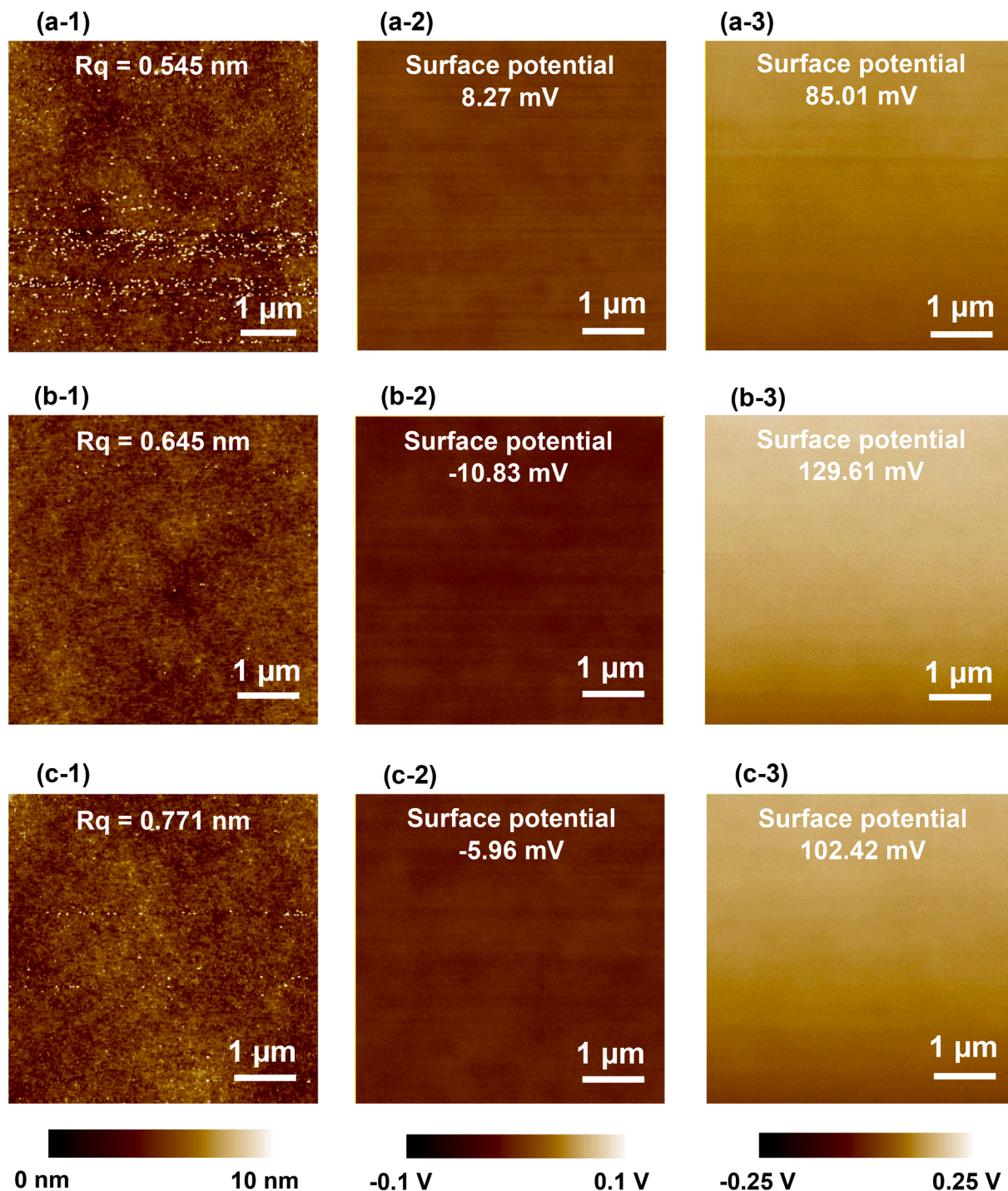


Fig. 5. Surface topographic images (a1 – c1) and surface potential mappings in the dark (a2 – c2) and under illumination (a3 – c3) of the three different PDMS@BTN nanocomposites: (a) PDMS@BTN-1, (b) PDMS@BTN-2, and (c) PDMS@BTN-3.

potential difference and eventually achieve electrostatic equilibrium. When the triboelectric layers return to the initial contact position from the maximum displacement state, electron transfer occurs in the reverse direction until complete contact. This releasing and pressing process can be repeated to collect triboelectric signals.

Under illumination, the as-fabricated TENGs execute a double conversion mechanism. Apart from the contribution from triboelectrification, photoexcited electron and hole generation is another origin of the electric output, as exhibited in Fig. S9f-j.

To further investigate the mechanism of TENG output signal enhancement under light illumination, photoassisted KPFM measure-

ments were performed to compare the PDMS@BTN nanocomposite layer work function variations between dark and illumination conditions, as shown in Table 2. We measured the surface potential of the as-prepared negative electrification layers with various amounts of BTNs embedded into the PDMS matrix in the dark and under illumination conditions (Fig. 5). The work function of the PDMS@BTN nanocomposite-based friction layer can be determined using the following equation [37]:

$$\text{CPD} = \frac{\phi_{\text{tip}} - \phi_{\text{sample}}}{e}$$

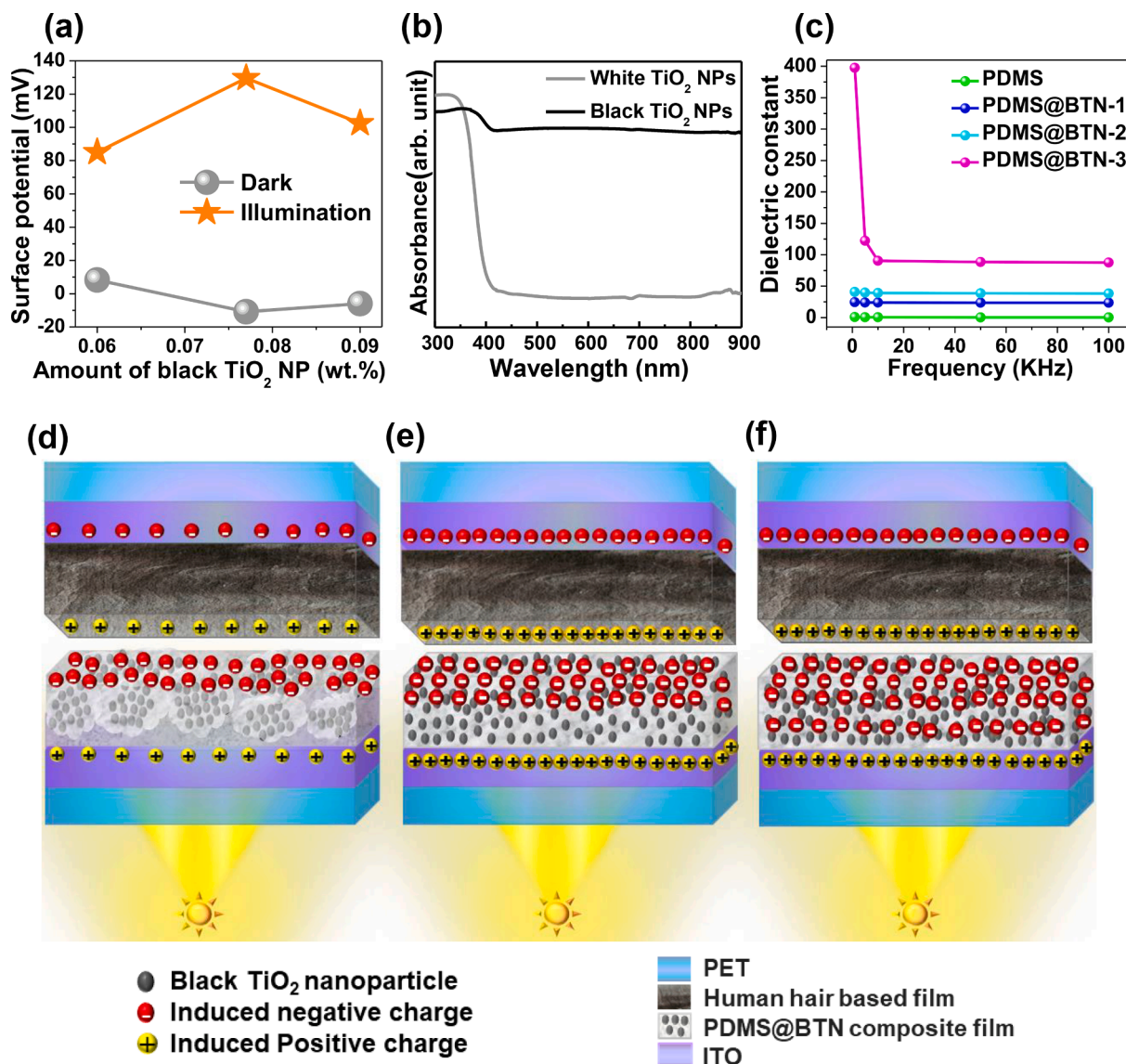


Fig. 6. (a) Surface potential variations of PDMS@BTN nanocomposite films with different BTN contents between dark and illumination conditions. (b) UV-vis absorption spectra of the BTNs and WTNs. (c) Dielectric constants of the PDMS@BTN nanocomposite films developed with different BTN concentrations as a function of frequency. Schematic diagram of the triboelectric charge transfer process in the TENGs based on the (d) PDMS@BTN-1 friction layer, (e) PDMS@BTN-2 friction layer and (f) PDMS@BTN-3 friction layer.

Table 2

Variations in the work function (WF) of the three different PDMS@BTN nanocomposites between dark and illumination conditions.

| Samples | WF in the dark (eV) | WF under illumination (eV) | Δ WF (eV) |
|------------|---------------------|----------------------------|------------------|
| PDMS@BTN-1 | 4.94 | 4.86 | -0.08 |
| PDMS@BTN-2 | 4.96 | 4.81 | -0.15 |
| PDMS@BTN-3 | 4.95 | 4.84 | -0.11 |

where ϕ_{tip} and ϕ_{sample} signify the work functions of the tip and sample, respectively, and e is the elementary charge ($1.602 \times 10^{-19}C$).

Illumination generates a large number of electron-hole pairs within the PDMS@BTN nanocomposite layer, and anatase BTNs serve as an origin of photogenerated electron pairs, with rutile BTNs acting as hole traps [38], whereas excess electrons then tend to be neutralized via

recombination by adsorbing positively charged ions or particles from the air [11]. This photoinduced hole trapping leading to an increase in the measured surface potential (Fig. 5, Fig. 6a), thus diminishing the work function [39], could induce electrons to move from the opposite electrification layer via the attractive force during triboelectrification [40], thus contributing to the intensified TENG output signal. As depicted in Fig. 5 and Table 2, PDMS@BTN-2 was again confirmed to be the best performing photoinduced negative electrification layer among all three PDMS@BTN nanocomposites by achieving the highest deviations in the measured surface potential (Fig. 6a) and calculated work function between dark and illumination conditions.

Upon light illumination, photoexcited electrons and holes were induced, and they could be simply trapped by the surface defects of highly photosensitive (Fig. 6b) BTNs [19] embedded in the negative electrification layer, thus serving as trapping sites. These photoexcited charges augment the preexisting triboelectric charges, eventually resulting in an elevation in the surface charge density that facilitates the performance of PDMS@BTN-2- and PDMS@BTN-3-based TENGs upon light illumination [16]. The three different fabricated TENGs have

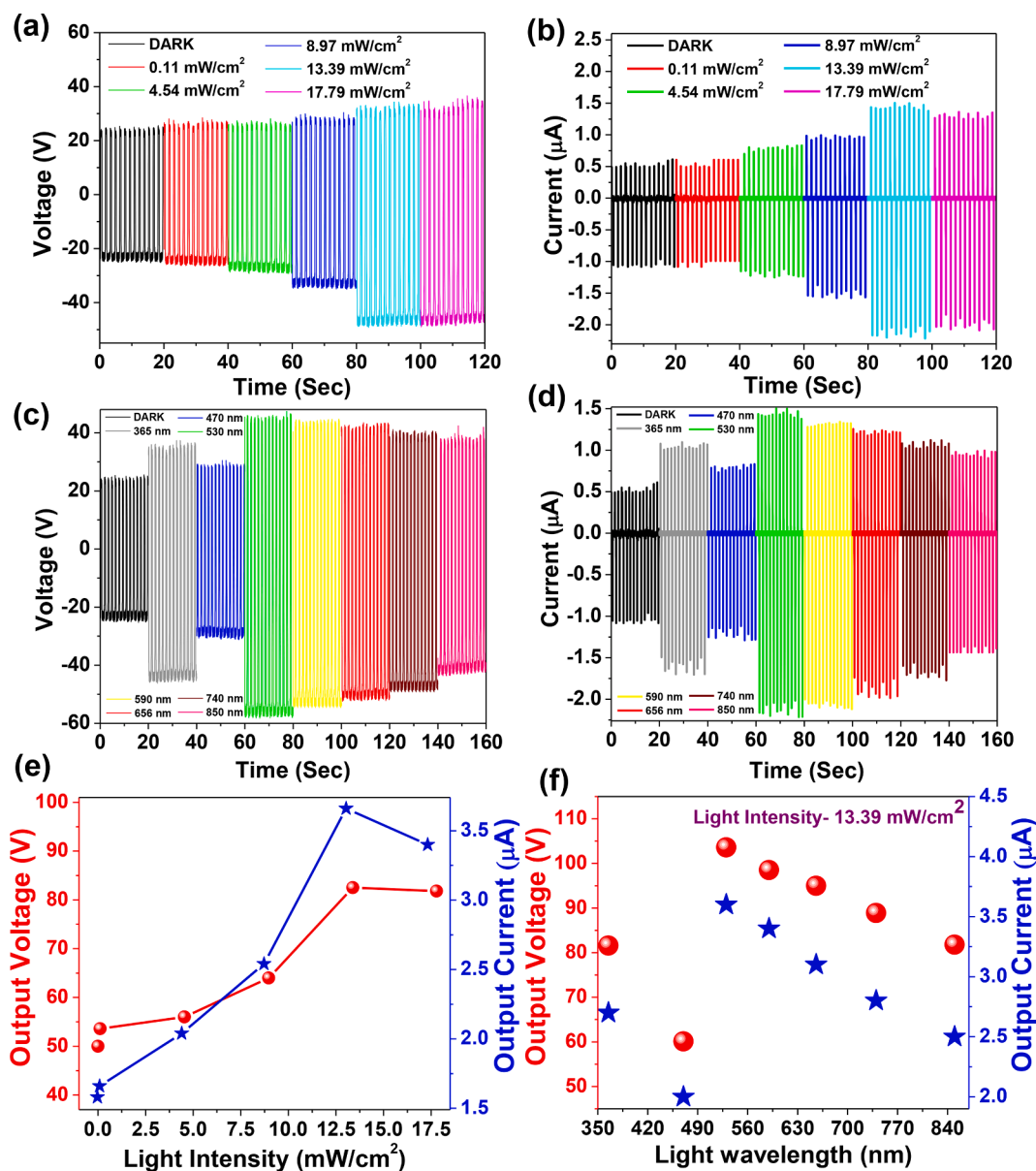


Fig. 7. Changes in output (a) voltage and (b) current signals of PDMS@BTN-2-based TENGs upon illumination (white light) with increasing intensity. Changes in the (c) voltage and (d) current outputs upon illumination that varies in wavelength. Variation in the TENG output signal under illumination with different (e) intensities and (f) wavelengths.

different photoinduced enhancement characteristics, which are mostly ascribed to the disparate interface actions on charge generation and transfer. Fig. 6d shows a simple mechanism by which BTNs, collected into clusters in different enclosures inside the PDMS matrix for the PDMS@BTN-1-based negative electrification layer (Fig. S1b), are not capable of directly interacting with light, resulting in the above-mentioned nonresponsive behavior of the PDMS@BTN-1-based TENG upon light illumination. The uniform distribution of BTNs within the PDMS matrix (Fig. 2m) and controlled enhancement of the dielectric constant of the electrification layer (Fig. 6c) work together to make the PDMS@BTN-2 nanocomposite film the best performing negative electrification layer (Fig. 6e) that achieved superior photoresponse characteristics, including the highest photoinduced enhancement and improved recovery time (18 s), among all PDMS@BTN nanocomposites. The PDMS@BTN-3-based TENG manifests a slightly longer response time (810–1000 ms) for the first response, which is probably due to the agglomeration of BTNs on the surface of the PDMS@BTN-3 nanocomposite layer, which diminishes the effective light interaction.

Additionally, this composite film suffers from a longer recovery time (91 s), which may be due to the dielectric hysteresis [41] caused by trapping of triboelectric charges into the deeper zone of the frictional layer (Fig. 6f) induced by the very high dielectric constant of the PDMS@BTN-3 nanocomposite layer (Fig. 6c). Fig. 4 also reveals the reduction in the mean peak-to-peak output voltage and current under illumination as the BTN content further increases to 0.09 wt%, which may again be caused by the agglomeration of BTNs on the surface of the PDMS@BTN-3 nanocomposite layer, as depicted by the FE-SEM analysis (Fig. S1c); this process can reduce the effective interaction of light with the BTNs.

Under identical conditions, the PDMS@WTN-based TENG shows almost nonreactive behavior, as shown in Fig. S10, indicating that the main influencing factor of the superior photoresponse of the PDMS@BTN-based TENG is the absorption behavior of BTNs exhibited over most of the UV, visible and near-IR regions ranging from 300 ~ 900 nm, while WTNs only show absorption behavior in the UV range [42], as confirmed in Fig. 6b.

The above results demonstrate that the as-fabricated PDMS@BTN-2-based TENG is highly photosensitive and can actually be considered a self-powered photodetector. The responses to various light intensities from 0 to 17.79 mW cm⁻² are presented in Fig. 7a, b, e, as the ability of a photodetector to reflect the intensity of the light is also important. The output signals show a significant uptrend with increasing light intensity, and three main stages are found. The response of the TENG output signal to light is usually an initial infinitesimal rise when the light intensity is less than 5 mW cm⁻², then a swift amplification with increasing intensity and finally a gradual saturation up to 17.79 mW cm⁻². The dependence of the TENG output signal on the illuminated light intensity enables the PDMS@BTN-2-based TENG to be a feasible technology for photodetection [43].

The eligibility of a photodetector is also characterized by an important parameter, the responsivity (R), which measures the electrical output per optical input [44] and can be evaluated by the following equation:

$$R = \frac{V_{light} - V_{dark}}{AP_{ill}}$$

where V_{light} and V_{dark} are the voltage amplitudes when the TENG-based photodetector is under illumination and in the dark, respectively. P_{ill} and A are the light intensity and the active illuminated area of the device, respectively. The active illuminated area of the device is the optimized effective area of the device illuminated during the data acquisition from the as-fabricated TENG device under illumination conditions. In the present study, this active illuminated area was approximately 4.45 cm². The responsivity (R) for white light with a 13.39 mW/cm² illumination intensity was obtained to be 606.8 V W⁻¹, which is orders of magnitude higher than that of modern TENG-based photodetectors [15,45].

The linear dynamic range (LDR) identifies the illumination intensity range over which the photoresponse of the device remains linear, and the LDR can be calculated using the equation [46,47].

$$LDR = 20 \log_{10} \frac{P_{max}}{P_{min}}$$

where P_{max} is the maximum illumination intensity where the photocurrent signal starts to deviate from linearity and P_{min} is the minimum value of detectable incident light intensity.

Now, considering the values of P_{max} and P_{min} extracted from the linear fitting curve demonstrated in Fig. S11, the LDR value for our device is calculated as.

$$LDR = 20 \log_{10} \frac{17.79}{0.11} = 44.176 \text{ dB}$$

Therefore, the as-fabricated TENG device can be concluded to represent an eco-friendly and self-powered photodetection approach with a wide wavelength range detection capacity and a capability to detect a reasonable intensity range that compare well with the present background of photodetection [48,49]. The lowest detection limit for the optimum photoinduced TENG is approximately 0.11 mW/cm², which compares well with that of a wide variety of photoinduced TENGs [15,45,50,51], while very few photoassisted TENGs with a reported lowest detection limit on the order of pW/cm²-μW/cm² exist, with the detection capability limited to over the UV region of the solar spectrum [52,53].

Additionally, as the broadband detection capacity is another major criterion for a photodetector [54], the variation in the output signal from the PDMS@BTN-2-based TENG at different monochromatic light wavelengths of 365, 470, 530, 590, 656, 740 and 850 nm, which cover the UV, visible and near-infrared (IR) regions, was also investigated, as shown in Fig. 7c, d, f. Regardless of the UV (i.e., wavelength less than 400 nm), visible (i.e., wavelength from approximately 400 nm to 750 nm), or near-IR (i.e., wavelength greater than 800 nm) region, the output signals exhibit significant changes under illumination, which

indicates an excellent broadband detection ability. This broadband detection capability represents a significant contribution to the recent advances in broadband photodetectors [45,55,56,57]. Among these wavelengths, monochromatic light of 530 nm induces the most elevated output signal, as shown in Fig. 7c,d, and the pattern of output signal variation with light wavelength can be elucidated by the fact that the visible part of the solar spectrum has a much higher intensity and a wider range than the UV part [15], which complies with the pattern of the UV-Vis absorption spectrum of the BTNs (Fig. 6b and Fig. S12). The slight decrease in the absorbance for BTNs above 400 nm demonstrated in Fig. 6b could be due to the mid-gap states introduced by oxygen vacancies. The BTN absorption shows a significant enhancement in the visible light region, which can be due to the introduction of oxygen vacancies and Ti³⁺ formation after calcination under an argon atmosphere, which is consistent with the changes in TiO₂ color from white to black [58-60].

In this research, the mixed-phase BTNs can be considered the optically active layer, and the as-synthesized BTNs with trivalent titanium ions, structural defects, and oxygen vacancies show remarkably high absorbance in the visible light spectrum. The oxygen vacancy defects (Ti³⁺ and Ti—O—H terminated bonding) act as trapping centers, and the existence of the trapping centers can efficiently reduce the recombination of electrons and holes [19,61]. The increased carrier lifetime contributes to the enhanced photoinduced signal intensification of the as-fabricated TENG. Fig. S13 and Table S3 reveal that the responsivity exhibits significant variation with the illumination wavelength while maintaining a pattern of variation that conforms to the UV-visible absorption spectrum of BTNs. The considerably high responsivity represents the superior optical-to-electrical conversion efficiency of the as-fabricated optimal TENG device, and the wavelength-dependent variation in the responsivity reveals the broadband detection capacity of this device.

Human hair plays two basic roles in this research. The first is improving the energy harvesting property of the TENG via the highly positive static electricity of hair and facilitating the effective light interaction of the PDMS@BTN-based negative tribolayer through the appreciable transparency of the human hair-based film, thereby maintaining the transparency of the whole TENG device. The second important role is that the utilization of waste human hair characterizes this TENG device as a very cost-efficient promising green energy source for the circular bioeconomy, thereby easing the difficulties in waste management systems and eliminating environmental pollution for socioeconomic welfare.

To evaluate the significance of human hair waste in this research, the output voltage and current were measured for TENGs based on PDMS@BTN-2 with a human hair film and an aluminum film, separately. Both the hair film and Al serve as positive tribolayers under dark and illumination conditions, keeping all other measurement conditions unaltered. As depicted in Fig. S14 a, b, the magnitude of the output signals and the photoinduced intensification are reduced by the use of Al as the positive tribolayer compared to the use of the hair film as the positive tribolayer. The lower performance of the Al-based positive tribolayer is possibly due to the fact that the hair-based tribolayer loses more electrons during the triboelectrification process than the Al-based tribolayer owing to the presence of a lipid layer on hair fibers, which is responsible for its strong positive static electricity [62], and due to the superior transparency of the hair film-based positive side of the TENG, which helps provide very effective light interactions to the PDMS@BTN-based negative tribolayer.

Fig. S15 presents convincing evidence that the untreated human hair waste exhibited output voltage and current signals close to those of the chemically treated human hair film. Thus, the PDMS@BTN-2 nanocomposite film is anticipated to effectually harvest natural hair movement as a result of spontaneous gestures, thereby fulfilling users' various operational needs and performing the abovementioned broadband photodetection under sunlight while affixed on the inner side of some

Table 3

Comparison of the photoinduced TENG output performance with that in other studies.

| Active material | Operation mode | Detection range | Responsivity/ Change in output | Ref. |
|--|----------------|-----------------|---|----------|
| CH ₃ NH ₃ PbI ₃ -PVDF | PENG | 462–630 nm | Reduction in voltage ~42 % (white light) | 55 |
| MAPbI ₃ perovskite | TENG | Not detected | Increase in voltage ~11 % (full sun) | 22 |
| MAPbI ₃ perovskite | TENG | 200–800 nm | Reduction in voltage ~37.5 % R = 7.5 V/W (full sun) | 15 |
| MAPb _x Cl _{3-x} perovskite | TENG | 365–780 nm | Increase in voltage ~55.7 % R = 119.3 V/W (full sun) | 45 |
| Bismuth oxyiodide | TENG | Not detected | Increase in voltage ~21 % (white light) | 17 |
| TiO ₂ /PANI | TENG | Not detected | Increase in voltage ~54.3 % (sunlight) | 63 |
| P3HT:PC ₆₁ BM | TENG | Not detected | Increase in voltage ~63 % (white light) | 64 |
| Black TiO ₂ NPs | TENG | 365–850 nm | Increase in voltage ~68 % (white light), R = 606.8 V/W | Our work |

transparent hair accessories, such as a hairband, a hair clip, a hair cap, a hairbrush, a head cap, and a helmet (Fig. 1).

To elucidate the significance of this research, the important results from the optimal photoinduced TENG were compared with those of the latest relevant reports based on photoinduced nanogenerators. As presented in Table 3, our photoinduced TENG based on the novel tribopair of PDMS@BTN-2 and a human hair film clearly compares well with those of previous relevant studies [15,17,22,45,55,63,64].

4. Conclusions

In summary, a biobased self-powered and ultrabroadband photodetector based on a PDMS@black TiO₂ nanocomposite film and a chemically treated human hair film was developed, in which the energy harvesting module and the sensing module were integrated. Under illumination, the optimal device based on the PDMS@BTN-2 nanocomposite film as a negative electrification layer achieved the largest photoinduced enhancement (1.7–2.2 times), with improvements in the response and recovery times compared to the other PDMS@black TiO₂ nanocomposite films under consideration in our investigation, as the output performance strongly depends on the content of BTNs embedded in the negative electrification layer. By investigating the mechanism, we found that the consequential increase in the photodetector performance is attributed to the efficacious charge separation induced by the photogenerated electron-hole pairs, which significantly changes the surface potential upon light illumination. These outcomes can contribute to the design of high-performance vibrating and solar energy harvesting devices as well as to the evolution of self-powered and ultrabroadband photodetectors with superior photoresponsivity (606.8 V W⁻¹), thus illustrating the concept of bioeconomic recycling for systematized management of hair waste as a regenerative resource in society and in nature.

CRedit authorship contribution statement

Ishita Chakraborty: Conceptualization, Formal analysis, Investigation, Methodology, Data curation, Writing – original draft. **Ming-Chung Wu:** Methodology, Formal analysis, Investigation, Writing – review & editing. **Sz-Nian Lai:** Investigation, Writing – review & editing. **Chao-Sung Lai:** Conceptualization, Funding acquisition, Project

administration, Writing – review & editing, Supervision.

Declaration of Competing Interest

The authors declare that they have no known competing financial interests or personal relationships that could have appeared to influence the work reported in this paper.

Data availability

Data will be made available on request.

Acknowledgments

The authors acknowledge the financial support provided by the Ministry of Science and Technology, Taiwan [grant numbers MOST109-2221-E-182-013-MY3, MOST110-2622-8-182-001-TS1, MOST110-2119-M-492-002-MBK] and Chang Gung Memorial Hospital Research Project [grant numbers CMRPD2K0171 and CORPD2J0072]. The authors also wish to thank the donors who donated their hair waste solely for the purpose of this research.

Appendix A. Supplementary data

Supplementary data to this article can be found online at <https://doi.org/10.1016/j.cej.2022.139138>.

References

- [1] Z.L. Wang, J. Chen, L. Lin, Progress in triboelectric nanogenerators as a new energy technology and self-powered sensors, *Energy Environ. Sci.* 8 (2015) 2250–2282, <https://doi.org/10.1039/C5EE01532D>.
- [2] J. Wang, J. He, L. Ma, Y. Yao, X. Zhu, L. Peng, X. Liu, K. Li, M. Qu, A humidity-resistant, stretchable and wearable textile-based triboelectric nanogenerator for mechanical energy harvesting and multifunctional self-powered haptic sensing, *Chem. Eng. J.* 423 (2021), 130200, <https://doi.org/10.1016/j.cej.2021.130200>.
- [3] B.U. Ye, S.Y. Lee, M. Jung, S.D. Sohn, H.J. Shin, M.H. Song, K.J. Choi, J.M. Baik, Photo-stimulated triboelectric generation, *Nanoscale* 9 (2017) 18597, <https://doi.org/10.1039/C7NR07020A>.
- [4] R.D.I.G. Dharmasena, S.R.P. Silva, Towards optimized triboelectric nanogenerators, *Nano Energy* 62 (2019) 530–549, <https://doi.org/10.1016/j.nanoen.2019.05.057>.
- [5] F.R. Fan, L. Lin, G. Zhu, W. Wu, R. Zhang, Z.L. Wang, Transparent triboelectric nanogenerators and self-powered pressure sensors based on micropatterned plastic films, *Nano Lett.* 12 (2012) 3109–3114, <https://doi.org/10.1021/nl300988z>.
- [6] P. Bai, G. Zhu, Y.S. Zhou, S. Wang, J. Ma, G. Zhang, Z.L. Wang, Dipole-moment-induced effect on contact electrification for triboelectric nanogenerators, *Nano Res.* 7 (2014) 990–997, <https://doi.org/10.1007/s12274-014-0461-8>.
- [7] Y. Liu, X. Wang, Y. Yan, Z. Rao, H. Chen, T. Guo, A novel post-processed surface modified double network polymer layer for a triboelectric nanogenerator, *J. Mater. Chem. A* 8 (2020) 6328, <https://doi.org/10.1039/D0TA01070G>.
- [8] J.M. Wu, C.K. Chang, Y.T. Chang, High-output current density of the triboelectric nanogenerator made from recycling rice husks, *Nano Energy* 19 (2016) 39–47, <https://doi.org/10.1016/j.nanoen.2015.11.014>.
- [9] G. Jian, Q. Meng, Y. Jiao, L. Feng, H. Shao, F. Wang, F. Meng, Hybrid PDMS-TiO₂-stainless steel textiles for triboelectric nanogenerators, *Chem. Eng. J.* 417 (2021), 127974, <https://doi.org/10.1016/j.cej.2020.127974>.
- [10] S. Cheon, H. Kang, H. Kim, Y. Son, J.Y. Lee, H.J. Shin, S.W. Kim, J.H. Cho, High-performance triboelectric nanogenerators based on electrospun polyvinylidene fluoride-silver nanowire composite nanofibers, *Adv. Funct. Mater.* 28 (2018) 1703778, <https://doi.org/10.1002/adfm.201703778>.
- [11] R. Wen, J. Guo, A. Yu, J. Zhai, Z.L. Wang, Humidity-resistive triboelectric nanogenerator fabricated using metal organic framework composite, *Adv. Funct. Mater.* 29 (2019) 1807655, <https://doi.org/10.1002/adfm.201807655>.
- [12] Z. Fang, K.H. Chan, X. Lu, C.F. Tan, G.W. Ho, Surface texturing and dielectric property tuning toward boosting of triboelectric nanogenerator performance, *J. Mater. Chem. A* 6 (2018) 52–57, <https://doi.org/10.1039/C7TA07696G>.
- [13] X. Zhang, S. Lv, X. Lu, H. Yu, T. Huang, Q. Zhang, M. Zhu, Synergistic enhancement of coaxial nanofiber-based triboelectric nanogenerator through dielectric and dispersivity modulation, *Nano Energy* 75 (2020), 104894, <https://doi.org/10.1016/j.nanoen.2020.104894>.
- [14] I. Chakraborty, S.N. Lai, J.M. Wu, C.S. Lai, α-Fe₂O₃ nanoparticles aided-dual conversion for self-powered bio-based photodetector, *Nanomaterials* 12 (2022) 1147, <https://doi.org/10.3390/nano12071147>.
- [15] L. Su, Z.X. Zhao, H.Y. Li, J. Yuan, Z.L. Wang, G.Z. Cao, G. Zhu, High-performance organolead halide perovskite-based self-powered triboelectric photodetector, *ACS Nano* 9 (2015) 11310–11316, <https://doi.org/10.1021/acs.nano.5b04995>.

- [16] J. Han, X. Yang, L. Liao, G. Zhou, G. Wang, C. Xu, W. Hu, M.E.R. Deborá, Q. Song, Photoinduced triboelectric polarity reversal and enhancement of a new metal/semiconductor triboelectric nanogenerator, *Nano Energy* 58 (2019) 331–337, <https://doi.org/10.1016/j.nanoen.2019.01.019>.
- [17] Z. Yu, H. Yang, N. Soin, L. Chen, N. Black, K. Xu, P.K. Sharma, C. Tsonos, A. Kumar, J. Luo, Bismuth oxyhalide based photo-enhanced triboelectric nanogenerators, *Nano Energy* 89 (2021), 106419, <https://doi.org/10.1016/j.nanoen.2021.106419>.
- [18] Y. Wu, J. Qu, P.K. Chu, D.M. Shin, Y. Luo, S.P. Feng, Hybrid photovoltaic-triboelectric nanogenerators for simultaneously harvesting solar and mechanical energies, *Nano Energy* 89 (2021), 106376, <https://doi.org/10.1016/j.nanoen.2021.106376>.
- [19] M.C. Wu, K.C. Hsiao, Y.H. Chang, S.H. Chan, Photocatalytic hydrogen evolution of palladium nanoparticles decorated black TiO₂ calcined in argon atmosphere, *Appl. Surf. Sci.* 430 (2018) 407–414, <https://doi.org/10.1016/j.apsusc.2017.08.071>.
- [20] M.C. Wu, I.C. Chang, K.C. Hsiao, W.K. Huang, Highly visible-light absorbing black TiO₂ nanocrystals synthesized by sol-gel method and subsequent heat treatment in low partial pressure H₂, *J. Taiwan Inst. Chem. Eng.* 63 (2016) 430–435, <https://doi.org/10.1016/j.jtice.2016.02.026>.
- [21] H. Li, L. Zhao, J. Meng, C. Pan, Y. Zhang, Y. Zhang, Z. Liu, Y. Zou, Y. Fan, Z. L. Wang, Z. Li, Triboelectric-polarization-enhanced high sensitive ZnO UV sensor, *Nano Today* 33 (2020), 100873, <https://doi.org/10.1016/j.nantod.2020.100873>.
- [22] L. Su, Z. Zhao, H. Li, Y. Wang, S. Kuang, G. Cao, Z.L. Wang, G. Zhu, Photoinduced enhancement of a triboelectric nanogenerator based on an organolead halide perovskite, *J. Mater. Chem. C* 4 (2016) 10395–10399, <https://doi.org/10.1039/C6TC03513B>.
- [23] I. Chakraborty, S.N. Lai, M.C. Wu, H.Y. Lin, C. Li, J.M. Wu, C.S. Lai, Charge trapping with α -Fe₂O₃ nanoparticles accompanied by human hair towards an enriched triboelectric series and a sustainable circular bioeconomy, *Mater. Horiz.* 8 (2021) 3149–3162, <https://doi.org/10.1039/D1MH00919B>.
- [24] E.N. Jayaweera, K.R. Wijewardhana, T.K. Ekanayaka, A. Shahzad, J.K. Song, Triboelectric Nanogenerator Based on Human Hair, *ACS Sustainable Chem. Eng.* 6 (2018) 6321–6327, <https://doi.org/10.1021/acssuschemeng.8b00136>.
- [25] M.A. Mujeeb, K.M. Zafar, ENERGY DISPERSIVE X-RAY ANALYSIS OF HUMAN HAIR, *International Journal of Science, Environment and Technology* 6 (2017) 2036–2040, <https://www.ijset.net/journal/1788.pdf>.
- [26] P. Ferreira, Á. Carvalho, T.R. Correia, B.P. Antunes, I.J. Correia, P. Alves, Functionalization of polydimethylsiloxane membranes to be used in the production of voice prostheses, *Sci. Technol. Adv. Mater.* 14 (2013), 055006, <https://doi.org/10.1088/1468-6996/14/5/055006>.
- [27] M.A. Amin, S.C. Dey, T.U. Rashid, M. Ashaduzzaman, S.M. Shamsuddin, Solar Assisted Photocatalytic Degradation of Reactive Azo Dyes in Presence of Anatase Titanium Dioxide, *International Journal of Latest Research in Engineering and Technology (IJLRET)* 2 (2016) 14–21, <http://www.ijlret.com/Papers/Vol-2-issu-e-3/14-B2016126.pdf>.
- [28] P. Garidel, H. Schott, Fourier-Transform Midinfrared Spectroscopy for Analysis and Screening of Liquid Protein Formulations, Part 1, *Bioprocess Int.* (2006) 40–46, in: http://www.bioprocessintl.com/wp-content/uploads/bpi-content/0605ar06_77561a.pdf.
- [29] M.A. Mujeeb, M.K.M. Zafar, FTIR Spectroscopic Analysis on Human Hair, *International Journal of Innovative Research in Science, Eng. Technol.* 6 (2017) 9327–9332, http://www.ijirset.com/upload/2017/may/195_43_FTIR-1.pdf.
- [30] J.G. Sun, T.N. Yang, I.S. Kuo, J.M. Wu, C.Y. Wang, L.J. Chen, A leaf-molded transparent triboelectric nanogenerator for smart multifunctional applications, *Nano Energy* 32 (2017) 180–186, <https://doi.org/10.1016/j.nanoen.2016.12.032>.
- [31] W. Seung, H.J. Yoon, T.Y. Kim, H. Ryu, J. Kim, J.H. Lee, J.H. Lee, S. Kim, Y.K. Park, Y.J. Park, S.W. Kim, Boosting Power-Generating Performance of Triboelectric Nanogenerators via Artificial Control of Ferroelectric Polarization and Dielectric Properties, *Adv. Energy Mater.* 7 (2017) 1600988, <https://doi.org/10.1002/aenm.201600988>.
- [32] A. Khalil, C. Dimas, R. Hashaikheh, Electrospun copper oxide nanofibers as infrared photodetectors, *Appl. Phys. A* 118 (2015) 217–224, <https://doi.org/10.1007/s00339-014-8820-6>.
- [33] W. Zheng, Y. Dong, T. Li, J.H. Chen, X. Chen, Y. Dai, G. He, MgO blocking layer induced highly UV responsive TiO₂ nanoparticles based self-powered photodetectors, *J. Alloy. Compd.* 869 (2021), 159299, <https://doi.org/10.1016/j.jallcom.2021.159299>.
- [34] M.R. Maurya, V. Toutam, D. Haranath, Comparative Study of Photoresponse from Vertically Grown ZnO Nanorod and Nanoflake Films, *ACS Omega* 2 (2017) 5538–5544, <https://doi.org/10.1021/acsomega.7b00914>.
- [35] A.D. Mahapatra, D. Basak, Biodegradable Filter Paper Based Broad-Band Photodetection by Chemical Bath Deposited SnS₂ 2D-Nanosheet Array Film, *ACS Appl. Electron. Mater.* 3 (2021) 2114–2122, <https://doi.org/10.1021/acsaem.1c00126>.
- [36] M. Sahoo, S.N. Lai, J.M. Wu, M.C. Wu, C.S. Lai, Flexible Layered-Graphene Charge Modulation for Highly Stable Triboelectric Nanogenerator, *Nanomaterials* 11 (2021) 2276, <https://doi.org/10.3390/nano11092276>.
- [37] M.C. Wu, S.H. Chan, K.M. Lee, S.H. Chen, M.H. Jao, Y.F. Chen, W.F. Su, Enhancing the efficiency of perovskite solar cells using mesoscopic zinc-doped TiO₂ as the electron extraction layer through band alignment, *J. Mater. Chem. A* 6 (2018) 16920, <https://doi.org/10.1039/C8TA05291C>.
- [38] M.C. Wu, K.C. Hsiao, Y.H. Chang, K. Kordás, Core–Shell Heterostructures of Rutile and Anatase TiO₂ Nanofibers for Photocatalytic Solar Energy Conversion, *ACS Appl. Nano Mater.* 2 (2019) 1970–1979, <https://doi.org/10.1021/acsnm.9b00005>.
- [39] H. Jiang, H. Lei, Z. Wen, J. Shi, D. Bao, C. Chen, J. Jiang, Q. Guan, X. Sun, S.T. Lee, Charge-trapping-blocking layer for enhanced triboelectric nanogenerators, *Nano Energy* 75 (2020), 105011, <https://doi.org/10.1016/j.nanoen.2020.105011>.
- [40] H.W. Park, N.D. Huynh, W. Kim, H.J. Hwang, H. Hong, K.H. Choi, A. Song, K. B. Chung, D. Choi, Effects of Embedded TiO_{2,x} Nanoparticles on Triboelectric Nanogenerator Performance, *Micromachines* 9 (2018) 407, <https://doi.org/10.3390/mi9080407>.
- [41] J. Wang, C. Wu, Y. Dai, Z. Zhao, A. Wang, T. Zhang, Z.L. Wang, Achieving ultrahigh triboelectric charge density for efficient energy harvesting, *Nat. Commun.* 8 (2017) 88, <https://doi.org/10.1038/s41467-017-00131-4>.
- [42] N.C. Hieu, T.M. Lien, T.T.T. Van, R.S. Juang, Enhanced removal of various dyes from aqueous solutions by UV and simulated solar photocatalysis over TiO₂/ZnO/rGO composites, *Sep. Purif. Technol.* 232 (2020), 115962, <https://doi.org/10.1016/j.seppur.2019.115962>.
- [43] J. Wang, K. Xia, J. Liu, T. Li, X. Zhao, B. Shu, H. Li, J. Guo, M. Yu, W. Tang, Z. Zhu, Self-powered silicon PIN photoelectric detection system based on triboelectric nanogenerator, *Nano Energy* 69 (2020), 104461, <https://doi.org/10.1016/j.nanoen.2020.104461>.
- [44] C.M. Yang, T.C. Chen, D. Verma, L.J. Li, B. Liu, W.H. Chang, C.S. Lai, Bidirectional All-Optical Synapses Based on a 2D Bi₂O₃Se/Graphene Hybrid Structure for Multifunctional Optoelectronics, *Adv. Funct. Mater.* 30 (2020) 2001598, <https://doi.org/10.1002/adfm.202001598>.
- [45] X.D. Yang, J.J. Han, G. Wang, L.P. Liao, C.Y. Xu, W. Hu, P. Li, B. Wu, A.M. Elsemán, G.D. Zhou, Q.L. Song, Robust perovskite-based triboelectric nanogenerator enhanced by broadband light and interface engineering, *J. Mater. Sci.* 54 (2019) 9004–9016, <https://doi.org/10.1007/s10853-019-03351-9>.
- [46] H. Ko, S. Park, H.J. Son, D.S. Chung, Wide-Linear-Dynamic-Range Polymer Photodiode with a New Benzo[1,2-b:4,5-b']dithiophene-Copolymer: The Role of Crystalline Orientation, *Chem. Mater.* 32 (2020) 3219–3228, <https://doi.org/10.1021/acs.chemmater.0c00347>.
- [47] B.R. Tak, R. Singh, Ultra-Low Noise and Self-Powered β -Ga₂O₃ Deep Ultraviolet Photodetector Array with Large Linear Dynamic Range, *ACS Appl. Electron. Mater.* 3 (2021) 2145–2151, <https://doi.org/10.1021/acsaem.1c00150>.
- [48] L. Dong, J. Yu, R. Jia, J. Hu, Y. Zhang, J. Sun, Self-powered MSM deep-ultraviolet β -Ga₂O₃ photodetector realized by an asymmetrical pair of Schottky contacts, *OPTICAL MATERIALS EXPRESS* 9 (2019) 3, <https://doi.org/10.1364/OME-9-001191>.
- [49] L. Dong, T. Pang, J. Yu, Y. Wang, W. Zhu, H. Zheng, J. Yu, R. Jia, Z. Chen, Performance-enhanced solar-blind photodetector based on a CH₃NH₃PbI₃/ β -Ga₂O₃ hybrid structure, *J. Mater. Chem. C* 7 (2019) 14205, <https://doi.org/10.1039/C9TC05115E>.
- [50] L. Shoostari, S. Ghods, R. Mohammadpour, A. Esfandiari, A. I. zad., Design of effective self-powered SnS₂/halide perovskite photo-detection system based on triboelectric nanogenerator by regarding circuit impedance, *Scientific Reports* 12 (2022) 7227, <https://doi.org/10.1038/s41598-022-11327-0>.
- [51] S. Singh, R.K. Tripathi, M.K. Gupta, G.I. Dzhardimalieva, I.E. Uflyand, B.C. Yadav, 2-D self-healable polyaniline-polypyrrole nanoflakes based triboelectric nanogenerator for self-powered solar light photo detector with DFT study, *J. Colloid Interface Sci.* 600 (2021) 572–585, <https://doi.org/10.1016/j.jcis.2021.05.052>.
- [52] Z.H. Lin, G. Cheng, Y. Yang, Y.S. Zhou, S. Lee, Z.L. Wang, Triboelectric Nanogenerator as an Active UV Photodetector, *Adv. Funct. Mater.* 24 (2014) 2810–2816, <https://doi.org/10.1002/adfm.201302838>.
- [53] L. Cheng, Y. Zheng, Q. Xu, Y. Qin, A Light Sensitive Nanogenerator for Self-Powered UV Detection with Two Measuring Ranges, *Adv. Optical Mater.* (2016), <https://doi.org/10.1002/adom.201600623>.
- [54] S.V.N. Pammi, R. Maddaka, V.D. Tran, J.H. Eom, V. Pecunia, S. Majumder, M. D. Kim, S.G. Yoon, CVD-deposited hybrid lead halide perovskite films for high-responsivity, self-powered photodetectors with enhanced photo stability under ambient conditions, *Nano Energy* 74 (2020), 104872, <https://doi.org/10.1016/j.nanoen.2020.104872>.
- [55] A. Sultana, P. Sadhukhan, M.M. Alam, S. Das, T.R. Middya, D. Mandal, Organo-Lead Halide Perovskite Induced Electroactive β -Phase in Porous PVDF Films: An Excellent Material for Photoactive Piezoelectric Energy Harvester and Photodetector, *ACS Appl. Mater. Interfaces* 10 (2018) 4121–4130, <https://doi.org/10.1021/acsaami.7b17408>.
- [56] A.D. Mahapatra, A. Das, S. Ghosh, D. Basak, Defect-Assisted Broad-Band Photosensitivity with High Responsivity in Au/Self-Seeded TiO₂ NR/Au-Based Back-to-Back Schottky Junctions, *ACS Omega* 4 (2019) 1364–1374, <https://doi.org/10.1021/acsomega.8b03084>.
- [57] S. Yang, S. Jiao, Y. Nie, H. Lu, S. Liu, Y. Zhao, S. Gao, D. Wang, J. Wang, Y. Li, A self-powered high performance UV-Vis-NIR broadband photodetector based on β -Bi₂O₃ nanoparticles through defect engineering, *J. Mater. Chem. C* 10 (2022) 8364–8372, <https://doi.org/10.1039/D1TC05646H>.
- [58] L. Shen, Z. Xing, J. Zou, Z. Li, X. Wu, Y. Zhang, Q. Zhu, S. Yang, W. Zhou, Black TiO₂ nanobelts/g-C₃N₄ nanosheets Laminated Heterojunctions with Efficient Visible-Light-Driven Photocatalytic Performance, *Sci. Rep.* 7 (2017) 41978, <https://doi.org/10.1038/srep41978>.
- [59] C. Zhao, D. Huang, J. Chen, DFT study for combined influence of C-doping and external electric field on electronic structure and optical properties of TiO₂ (001) surface, *J. Materiomics* 4 (2018) 247–255, <https://doi.org/10.1016/j.jmat.2018.05.003>.
- [60] T.S. Rajaraman, S.P. Parikh, V.G. Gandhi, Black TiO₂: A review of its properties and conflicting trends, *Chem. Eng. J.* 389 (2020), 123918, <https://doi.org/10.1016/j.cej.2019.123918>.

- [61] M.C. Wu, C.H. Chen, W.K. Huang, K.C. Hsiao, T.H. Lin, S.H. Chan, P.Y. Wu, C.F. Lu, Y.H. Chang, T.F. Lin, K.H. Hsu, J.F. Hsu, K.M. Lee, J.J. Shyue, K. Kordás, W.F. Su, Improved Solar-Driven Photocatalytic Performance of Highly Crystalline Hydrogenated TiO₂ Nanofibers with Core-Shell Structure, *Sci. Rep.* 7 (2017) 40896, <https://doi.org/10.1038/srep40896>.
- [62] D.W. Kim, S.W. Kim, U. Jeong, Lipids: Source of Static Electricity of Regenerative Natural Substances and Nondestructive Energy Harvesting, *Adv. Mater.* (2018) 1804949, <https://doi.org/10.1002/adma.201804949>.
- [63] S. Liu, X. Liu, G. Zhou, F. Qin, M. Jing, L. Li, W. Song, Z. Sun, A high-efficiency bioinspired photoelectric-electromechanical integrated nanogenerator, *Nat. Commun.* 11 (2020) 6158, <https://doi.org/10.1038/s41467-020-19987-0>.
- [64] M. Li, L. Yang, H. Wang, C. Qin, J. Song, Y. Zhang, W. Wang, Y. Wu, X. Zhang, H. Zheng, Coupling mechanism between photogenerated carriers and triboelectric charges and photoinduced reinforcement of a triboelectric nanogenerator, *Appl. Phys. Lett.* 119 (2021), 063903, <https://doi.org/10.1063/5.0059584>.